











RESEARCH ARTICLE

Prepolarized MRI of hard tissues and solid-state matter

Jose Borreguero Morata¹  | José M. González¹  | Eduardo Pallás^{2,3}  |
Juan P. Rigla¹  | José M. Algarín^{2,3}  | Rubén Bosch¹  | Fernando Galve^{2,3}  |
Daniel Grau-Ruiz¹ | Rubén Pellicer^{2,4}  | Alfonso Ríos¹ | José M. Benlloch^{2,3}  |
Joseba Alonso^{2,3} 

¹Tesoro Imaging S.L., Valencia, Spain

²MRILab, Institute for Molecular Imaging and Instrumentation (i3M), Spanish National Research Council (CSIC) and Universitat Politècnica de València (UPV), Valencia, Spain

³Instituto de Instrumentación para Imagen Molecular, Centro Mixto CSIC–Universitat Politècnica de València, Valencia, Spain

⁴Asociación de investigación MPC, San Sebastián, Spain

Correspondence

Jose Borreguero Morata, Tesoro Imaging S.L.,
46022 Valencia, Spain.

Email: pepe.morata@tesoroimaging.com

Funding information

Agència Valenciana de la Innovació; European Regional Development Fund; Ministerio de Ciencia e Innovación; This work was supported by the Ministerio de Ciencia e Innovación of Spain through research grant

PID2019-111436RBC21. Action co-financed by the European Union through the Programa Operativo del Fondo Europeo de Desarrollo Regional (FEDER) of the Comunitat Valenciana 2014-2020 (IDIFEDER/2018/022). JMG and JB acknowledge support from the Innoducto program of the Agencia Valenciana de la Innovación (INNTA3/2020/22 and INNTA3/2021/17); Ministerio de Ciencia e Innovación of Spain, Grant/Award Number: PID2019-111436RB-C21; Programa Operativo del Fondo Europeo de Desarrollo Regional (FEDER) of the Comunitat Valenciana, Grant/Award Number: IDIFEDER/2018/022; Innoducto program of the Agencia Valenciana de la Innovación, Grant/Award Numbers: INNTA3/2020/22, INNTA3/2021/17

Prepolarized MRI (PMRI) is a long-established technique conceived to counteract the loss in signal-to-noise ratio (SNR) inherent to low-field MRI systems. When it comes to hard biological tissues and solid-state matter, PMRI is severely restricted by their ultra-short characteristic relaxation times. Here we demonstrate that efficient hard-tissue prepolarization is within reach with a special-purpose 0.26 T scanner designed for ex vivo dental MRI and equipped with suitable high-power electronics. We have characterized the performance of a 0.5 T prepolarizer module, which can be switched on and off in 200 μ s. To this end, we have used resin, dental and bone samples, all with T_1 times of the order of 20 ms at our field strength. The measured SNR enhancement is in good agreement with a simple theoretical model, and deviations in extreme regimes can be attributed to mechanical vibrations due to the magnetic interaction between the prepolarization and main magnets.

KEYWORDS

MRI, low field, prepolarization, hard tissues, solid state

Abbreviations: ART, algebraic reconstruction technique; FID, free induction decay; GPA, gradient power amplifier; LF-MRI, low-field MRI; PETRA, pointwise encoding time-reduction with radial acquisition; PMRI, prepolarized MRI; P-PETRA, prepolarized pointwise encoding time-reduction with radial acquisition; SNR, signal-to-noise ratio; ZTE, zero echo time.

* JB and JMG contributed equally to this work.

This is an open access article under the terms of the [Creative Commons Attribution-NonCommercial](https://creativecommons.org/licenses/by-nc/4.0/) License, which permits use, distribution and reproduction in any medium, provided the original work is properly cited and is not used for commercial purposes.

© 2022 The Authors. *NMR in Biomedicine* published by John Wiley & Sons Ltd.

1 | INTRODUCTION

Low-field MRI (LF-MRI) is gaining momentum as an affordable alternative to clinical MRI, the current gold standard in numerous medical imaging applications, but also extremely expensive and often inaccessible.¹⁻³ The main cost driver in an MRI scanner is the superconducting magnet required to generate the strong, static magnetic field (B_0) that enables the high-quality images typical for clinical MRI. By lowering the field strength, the need for superconducting magnets is removed, resulting in a drastic reduction of the economic and energetic needs. On the other hand, the signal-to-noise ratio (SNR) of the magnetic resonance signals and reconstructed images depends supra-linearly on field strength ($\propto B_0^{3/2}$, Reference²), leading to longer scan times if resolution and SNR are to be maintained.

Prepolarization is a long-established technique designed to partially compensate for the SNR loss in LF-MRI⁴⁻⁸ and could be of special relevance for hard biological tissues, where hydrogen content is sparse and signals decay very fast.^{9,10} In prepolarized MRI (PMRI), the Boltzmann equilibrium magnetization of the sample is boosted by an intense, not necessarily homogeneous, magnetic pulse of amplitude B_p before the start of the imaging pulse sequence, which is then executed at a lower but highly homogeneous B_0 . For efficient PMRI, the prepolarization pulse must be turned off in a time t_{off} much shorter than the sample T_1 relaxation time over which the extra magnetization is lost. This is easily met for liquids and soft biological tissues, where spin-lattice interactions are averaged out by the molecular tumbling of water, leading to relaxation times above 100 ms.¹¹ Indeed, PMRI has already demonstrated its potential for ex vivo and in vivo imaging of soft samples at field strengths ranging from hundreds of millitesla to hundreds of microtesla.^{10,12-16} For solid-state matter or hard biological tissues (e.g., dental tissues), which feature short T_1 times, prepolarization is much more challenging: the suppressed proton mobility prevents the averaging out of dipolar interactions by molecular tumbling of protons in water. This effect is even more pronounced at low field strengths, where the Larmor frequency is closer to proton tumbling frequencies.¹⁷ These challenges have so far precluded PMRI of short- T_1 samples, which include tendons and bones,^{18,19} myelin,²⁰ lungs²¹ and teeth.^{9,22,23}

In this paper, we demonstrate prepolarization and imaging of samples with ultra-short T_1 , down to a few tens of milliseconds. After brief introductions to the relevant theoretical framework and experimental equipment in Sections 2 and 3 respectively, we analyze in Section 4 the signal strength boost for an inorganic solid-state sample as a function of pulse sequence parameters. In Section 5, we present the first prepolarized magnetic resonance hard-tissue images (of a cattle bone and a human tooth), which show an SNR increase of a factor of 2 with respect to an equivalent acquisition without prepolarization.

2 | THEORY

To quantify the effect of the prepolarization on hard tissues, in the remainder of the paper we compare the signals resulting from magnetic pulse sequences based on those in Figure 1. These sequences are identical except for the fact that the prepolarization pulse has an amplitude B_p in the

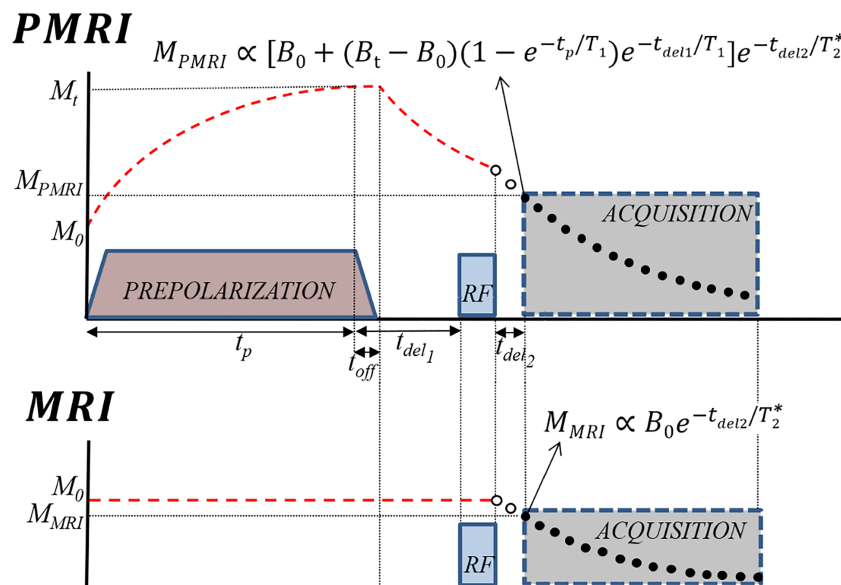


FIGURE 1 PMRI (top) and MRI (bottom) pulse sequences used in this work, with analytical expressions for the magnetization at the start of FID acquisition. Their ratio α represents the SNR gain due to prepolarization, as per Equation (2). M_t and M_0 are the magnetizations in thermal equilibrium with and without prepolarization and are directly proportional to B_t and B_0 respectively. Red dashed lines represent the longitudinal magnetization. Black points represent k -space data measured during the acquisition, while white points are not measured and lead to a gap in k space

PMRI sequence and zero in the standard MRI sequence. For an homogeneous sample of characteristic relaxation time T_1 , we define the prepolarization gain α as the ratio between the sample magnetizations during the data acquisitions:

$$\begin{aligned} M_{\text{PMRI}} &\propto (B_0 + (B_t - B_0)(1 - e^{-t_p/T_1})e^{-t_{\text{del1}}/T_1})e^{-t_{\text{del2}}/T_2^*}, \\ M_{\text{MRI}} &\propto B_0 e^{-t_{\text{del2}}/T_2^*}, \end{aligned} \quad (1)$$

so

$$\alpha \equiv \frac{M_{\text{PMRI}}}{M_{\text{MRI}}} = 1 + \frac{B_t - B_0}{B_0} (1 - e^{-t_p/T_1})e^{-t_{\text{del1}}/T_1}, \quad (2)$$

where we neglect the duration of RF pulses. Here $B_t = |\mathbf{B}_0 + \mathbf{B}_p|$ is the total field strength during the prepolarization pulse, where the main and prepolarization fields need not be parallel; t_p is the prepolarization pulse length, during which the magnetization asymptotically reaches equilibrium with B_t ; t_{off} is the ramp-down time of the prepolarization pulse; $t_{\text{del1}} \geq t_{\text{off}}$ is the time from the moment the prepolarization pulse starts to be switched off until the beginning of the RF excitation; t_{del2} is the time between the RF pulse and the start of the data acquisition and T_2^* is the sample- and scanner-dependent dephasing characteristic time over which the magnetization decoheres. Admittedly, this definition of SNR enhancement tends to overestimate the benefits of PMRI, since the standard MRI sequence could be shortened and its SNR increased by further averaging in the same overall acquisition time, as discussed in Section 6. Nevertheless, this is the simplest possible comparison and it is often used as a reference (see, e.g., References ^{12,24}).

3 | APPARATUS

As a result of the short T_1 timescales typical of solids, hard-tissue prepolarization poses a significant engineering challenge to achieve fast enough t_{off} times. Our solution to this follows.

The “DentMRI—Gen I” 0.26 T scanner, RF transmission and reception (Tx/Rx) coil and prepolarization modules employed for this work (see Figure 2) are described in detail elsewhere.^{9,10} Essentially, our group has designed, built and characterized a prepolarizer coil with inductance $L \approx 600\mu\text{H}$, resistance $R \approx 75\text{m}\Omega$ and efficiency $\eta \approx 1.9\text{mT/A}$. The gap between the planar gradient stacks is $\approx 210\text{mm}$, placing a hard boundary on the prepolarizer module size and, consequently, on the maximum achievable coil inductance. Due to geometric limitations, and to ease accessibility, we placed the prepolarizer module so that \mathbf{B}_p is perpendicular to \mathbf{B}_0 .¹⁰ This reduces the maximum achievable B_t from $|\mathbf{B}_0| + |\mathbf{B}_p|$ to $(B_0^2 + B_p^2)^{1/2}$, but has the advantage that the generated eddy currents and the residual energy in the prepolarization coil barely disturb the longitudinal field \mathbf{B}_0 (e.g., when B_p falls to 1 mT, the total field deviates from the original B_0 by only $2\mu\text{T}$).

In order to cope with the short T_1 of hard biological tissues, the high-power electronics setup for the prepolarizer module has been substantially upgraded with respect to the system introduced in Reference ¹⁰. In the current apparatus, a digital output from the RadioProcessor-G board

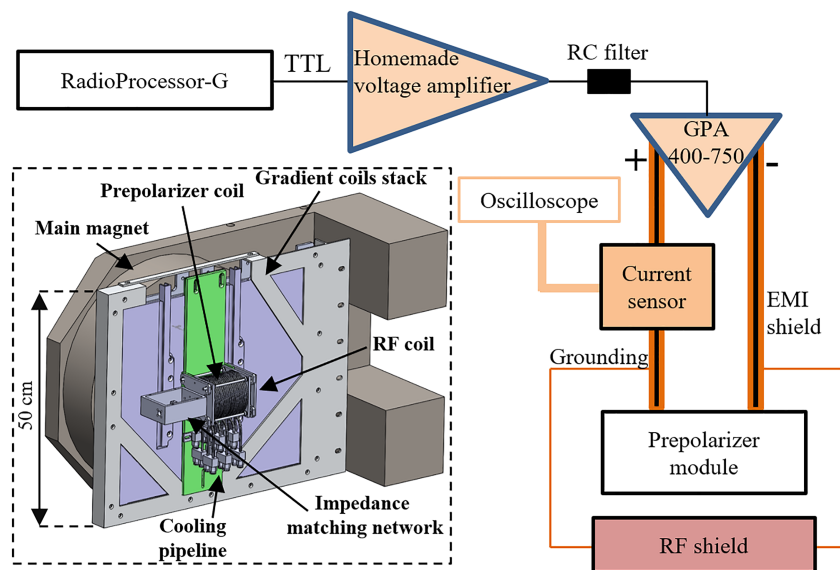


FIGURE 2 Schematic and CAD of the setup employed for hard-tissue PMRI. Further details of the apparatus are provided in References ^{9,10}

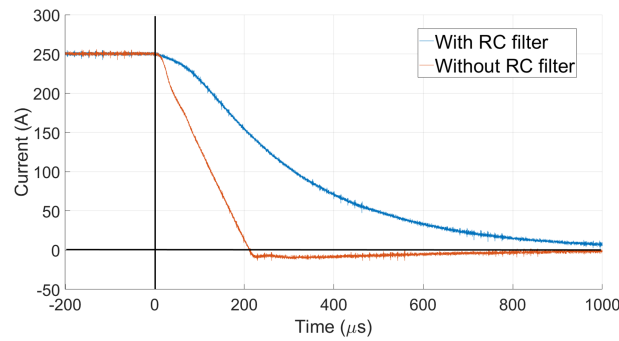


FIGURE 3 Falling edge of the prepolarization pulse current from 250 A ($B_p \approx 0.475$ T) with the GPA 400-750, with and without the low-pass RC filter. With the RC filter, the prepolarizer field is 15.6 mT after approximately 1 ms (1 mT at approximately 1.73 ms)

(SpinCore Electronics) is amplified in two stages, first in a home-made variable-gain low-voltage amplifier, and then in a high-power (400 A and 750 V) gradient power amplifier from International Electric Co. (GPA 400-750). The latter can ramp currents from 0 to ± 260 A in about 200 μ s in our approximately 600 μ H load, where we were previously limited to about 35 ms.¹⁰ Figure 3 also shows a smoother transition corresponding to the case where we low-pass filter the digital output with an RC circuit of characteristic time constant approximately 350 μ s. We have found this necessary to avoid significant mechanical displacements in the module due to the sudden appearance of strong magnetic interactions between the main magnet and the prepolarizer. This also reduces the generation of eddy currents and, thereby, distortions in the acquired signals and image reconstructions due to uncontrolled magnetic field dynamics. All the measurements below are with the low-pass filter.

4 | SNR ENHANCEMENT

For calibration and first tests we employed a sample made of a photopolymer resin,²⁵ which is highly homogeneous, abundant in hydrogen and features relaxation parameters comparable to the enamel in human teeth. At our B_0 , we have measured $T_1 \approx 23.1$ ms and $T_2 \approx 650$ μ s with inversion recovery²⁶ and CPMG^{27,28} pulse sequences, respectively.

In a first set of experiments we check whether the SNR is enhanced by prepolarization as predicted by the model in Equation (2). To this end, we set $t_p = 160$ ms ($> 7T_1$) in the sequence in Figure 6 to prepolarize close to the saturation magnetization. Next, a resonant $\pi/2$ RF pulse coherently rotates the magnetization to the transverse plane (RF pulse time $t_{RF} \approx 10$ μ s, with amplitude $B_1 \approx 590$ μ T). The two pulses are separated by a wait time $t_{del1} = 3$ ms, longer than strictly required to switch B_p off, to avoid Larmor frequency shifts and distortions in the acquired free induction decay (FID) signals due to residual magnetic energy in the setup. The signal readout starts $t_{del2} = 100$ μ s after the RF pulse to avoid ring-down from the RF coil. The resulting FID is acquired for $t_{acq} = 2$ ms with a readout bandwidth $BW = 200$ kHz. This protocol is repeated for four different voltage gains of our home-made amplifier, generating $B_p \approx 0.21, 0.29, 0.40$ and 0.49 T, which correspond to $B_t \approx 0.33, 0.39, 0.47$ and 0.56 T. Figure 4 shows the absolute values of the FIDs for these cases and for the standard MRI sequence ($B_p = 0$ and $B_t \approx 0.26$ T). For a given value of B_p , we estimate the prepolarization boost α as the mean ratio of the PMRI and standard MRI data:

$$\frac{1}{N_{\text{points}}} \sum_{i=1}^{N_{\text{points}}} \frac{s_{B_p}(t_i)}{s_0(t_i)}, \quad (3)$$

where $N_{\text{points}} = t_{\text{acq}} \cdot BW$, $s_{B_p}(t_i)$ is the signal amplitude measured for the PMRI with prepolarization strength B_p for the time bin (t_i), and $s_0(t_i)$ is the amplitude measured for the standard MRI sequence at t_i . The values of α estimated by this procedure are $1.240 \pm 0.005, 1.430 \pm 0.008, 1.705 \pm 0.008$ and 1.964 ± 0.011 for the above prepolarization field strengths, where the given uncertainties indicate the standard error of the mean

$$\sigma_\alpha = \frac{1}{N_{\text{points}}} \sqrt{\sum_{i=1}^{N_{\text{points}}} \left(\frac{s_{B_p}(t_i)}{s_0(t_i)} - \alpha \right)^2}. \quad (4)$$

The corresponding theoretical α values for $T_1 \approx 23.1$ ms can be calculated from Equation (2): $\alpha \approx 1.24, 1.44, 1.72$ and 1.98 .

The small experimental deviations from the theoretically calculated values could arise from (i) mechanical vibrations due to magnetic forces, (ii) induced eddy currents, (iii) off-resonant spin evolution due to a time-dependent Larmor frequency or (iv) dependence of T_1 on B_t . All four are more pronounced for intense B_p values and short t_{del1} times. To find a working regime where these effects are suppressed, we have characterized their influence on the SNR gain with the measurements shown in Figure 5.

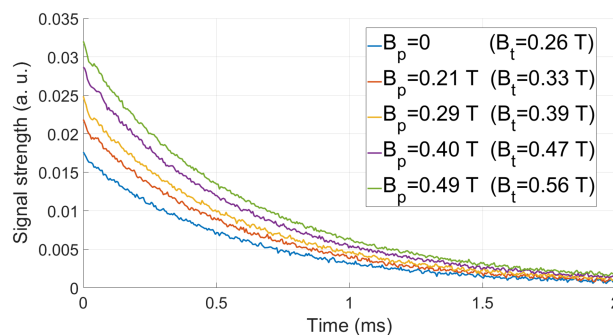


FIGURE 4 FIDs after prepolarizing the photopolymer resin sample with pulses of $t_p = 160$ ms and $t_{del1} = 3$ ms for different B_p values

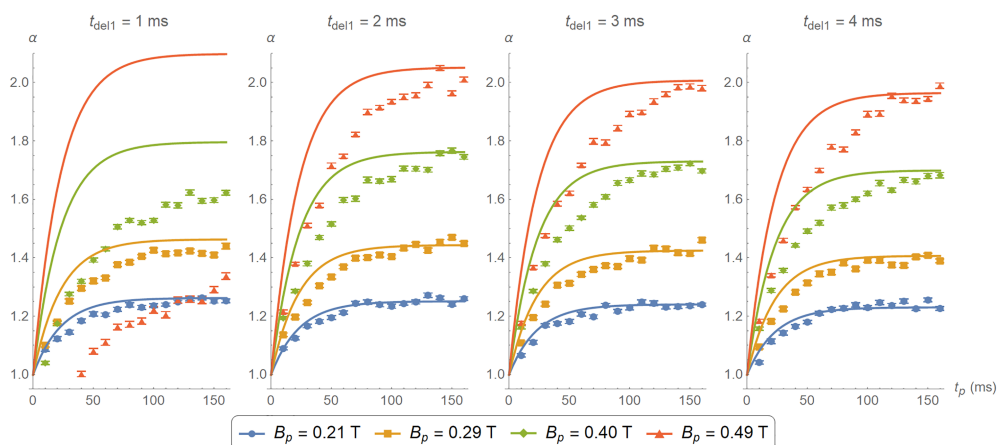


FIGURE 5 Comparison between theoretical (continuous curves) and experimentally estimated (data points) gain α for different values of t_p , B_p and t_{del1} , using the photopolymer resin sample. The data for $B_p = 0.49$ T and $t_{del1} = 1$ ms are heavily corrupted by the sharp magnetic transitions. The experimental data for the stronger B_p seem to grow more slowly than the corresponding theoretical curves, consistent with longer T_1 at higher field strengths

For the plots in Figure 5 we sweep the prepolarization pulse duration from $t_p = 10$ to 160 ms and t_{del1} from 1 to 4 ms, for the same four B_p values as above. The gain and uncertainty for every data point are estimated according to Equations (3) and (4). The solid lines in the figure correspond to calculations employing the model in Equation (2).

Unsurprisingly, for the weaker prepolarization currents we measure FID curves that follow closely theoretical predictions, even for t_{del1} as short as 1 ms. Deviations are stronger for short wait and prepolarization times. In the extreme case of $B_p \approx 0.49$ T and $t_{del1} = 1$ ms, the measured data were heavily corrupted and did not follow the typical exponential behavior (i.e., as in the FIDs in Figure 4). Moreover, the curve for $B_p \approx 0.4$ T is lower for $t_{del1} = 1$ ms than for $t_{del1} = 2$ ms. It is unlikely that these issues are due to drifts in the Larmor frequency as the prepolarizer relaxes, since a residual orthogonal field perturbs B_0 very weakly (e.g., for $B_p \approx 0.49$ T and $t_{del1} = 1$ ms, the Larmor frequency shifts by only 250 Hz). On the other hand, eddy currents and especially mechanical vibrations could be behind the aforementioned deviations. In fact, we have observed that these unwanted effects are more prominent if the prepolarizer is not rigidly fixed to the scanner. With the mechanical fixation in place (see Figure 2), the system performs well away from this extreme regime. A further deviation from theory occurs for higher B_p values, probably because at these B_t fields T_1 is higher than the one we have measured at B_0 . All in all, the plots in Figure 5 demonstrate that the measured SNR gain is compatible with theoretical predictions for prepolarization pulses longer than 120 ms and $t_{del1} \geq 2$ ms.

5 | HARD TISSUE PMRI

In this section we demonstrate the system's capability for imaging hard biological tissues with PMRI. To this end, we employ (i) an adult human molar tooth (Figure 7(c)) extracted one year before these experiments and dried so that primarily mineralized matter (dentin and enamel) remains and (ii) a piece of cattle rib (Figure 8(c)) including cortical and spongy bone tissues. We have measured the T_1 times of both samples by inversion recovery at B_0 in our system, and found $T_1 \approx 20.3$ and 19.3 ms for the tooth and bone, respectively. Using CPMG we have obtained $T_2 \approx 308 \mu\text{s}$ and 200 μs . The cattle bone contains both cortical and spongy tissues, so the estimated T_1 is an averaged quantity. The T_1 times of all the

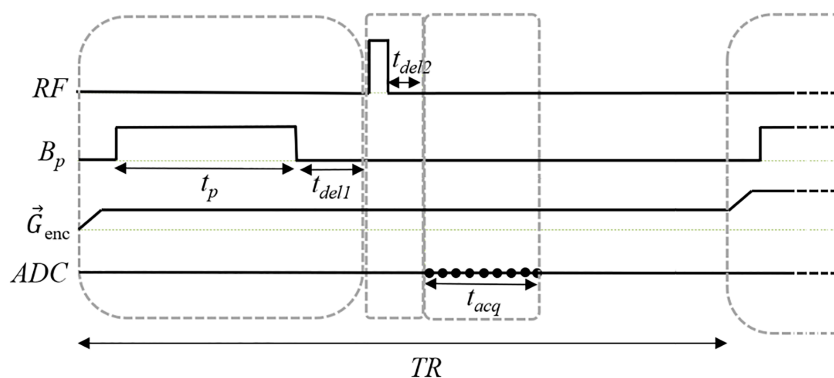


FIGURE 6 P-PETRA pulse sequence integrating the PMRI sequence in Figure 1 with PETRA. P-PETRA is employed for the prepolarized hard-tissue images in Figs. 7 and 8. Here, G_{enc} represents the (radial or pointwise) encoding gradient, and the ADC (analog-to-digital converter) acquisition is marked with black points. For pointwise encoding, only the first point in the acquisition is used

employed samples are very similar, so we can determine suitable parameter regimes from the measurements on the photopolymer resin (Figure 5).

The ultra-short T_2 times typical of hard tissues impose the use of dedicated MRI sequences, such as those in the zero echo time (ZTE) family.²⁹ These are characterized by radial k -space acquisitions beginning immediately after the RF excitation, to capture as much as possible of the short-lived signal. Ramping the gradient is time consuming, so in ZTE sequences the spatial encoding gradients are switched on before the RF pulse. In this work, we even switch on the frequency encoding gradient before prepolarization³⁰ to limit mechanical vibrations and the influence of eddy currents during data acquisition. Having the gradient on during resonant excitation imposes the use of hard (short and intense) RF pulses, leading to spurious signals, which could corrupt the data acquisition. To prevent this, we introduce a delay $t_{\text{del}2}$ before the readout, resulting in a gap without data at the center of k space. This can be filled with additional acquisitions.³¹ One possibility is to do so in a pointwise fashion, as in PETRA (pointwise encoding time-reduction with radial acquisition)³². For the following images we employ a PETRA sequence with a prepolarization stage before the RF excitation (P-PETRA, Figure 6).

In Figure 7 we show prepolarized images of a human molar tooth obtained following the scheme in Figure 6. The size of the field of view is set to $21 \times 13 \times 13 \text{ mm}^3$ and the image is reconstructed with algebraic reconstruction techniques (ARTs^{9,33,34}) into $42 \times 26 \times 26$ voxels. The acquisition has a bandwidth $\text{BW} \approx 30 \text{ kHz}$, it starts $t_{\text{del}2} = 130 \mu\text{s}$ after the RF pulse ($t_{\text{RF}} \approx 10 \mu\text{s}$) to avoid the effect of ring-down and it lasts $t_{\text{acq}} = 700 \mu\text{s}$. The repetition time is set to $T_{\text{R}} = 250 \text{ ms}$, limited by the maximum duty cycle of the GPA 400-750 at this current regime. We use 446 radial spokes for each of the 16 vertical planes, corresponding to a total k -space undersampling factor[†] of ≈ 8 with respect to the Nyquist criterion, where ART reconstructions are still robust, with 136 single Cartesian points in the center. Every image contains 12 averages for a total scan time of approximately 29 min. The bottom row of images in Figure 7A corresponds to scans in which a prepolarization pulse is triggered with a current intensity of approximately 260 A ($B_{\text{t}} \approx 0.56 \text{ T}$), which lasts $t_{\text{p}} = 90 \text{ ms}$ and where $t_{\text{del}1} = 2 \text{ ms}$. The pulse sequence for the top row of Figure 7A is identical, but the prepolarization pulse is not triggered ($B_{\text{p}} = 0, B_{\text{t}} = 0.26 \text{ T}$). The brightness scale is common to the two datasets. Both images have been denoised using a block-matching filter.^{9,35} To quantify the influence of prepolarization, we plot in Figure 7B the same profile along a horizontal line around the upper portion of the images in A, in the region of the tooth crown. We estimate the prepolarization boost α as the ratio $\text{SNR}_{\text{PMRI}}/\text{SNR}_{\text{MRI}}$, which we average over a region of interest of constant bright pixels around the dentin before filtering (red boxes in Figure 7A). This yields approximately 1.94, where $\text{SNR}_{\text{PMRI}} = \bar{s}_{\text{PMRI}}/\bar{n}_{\text{PMRI}} \approx 22.97$, and SNR_{MRI} (analogously defined) is approximately 11.84. The mean signal and noise values (\bar{s} and \bar{n}) are estimated, respectively, as the mean value and standard deviation of the voxel brightness in these regions. For comparison, the expected prepolarization gain from Equation (2) is approximately 2.02.

We have applied an analogous protocol to image a piece of a cattle rib bone. The size of the field of view is set to $36 \times 15 \times 15 \text{ mm}^3$ and the image is reconstructed with ART into $72 \times 30 \times 30$ voxels. The acquisition starts $t_{\text{del}2} = 125 \mu\text{s}$ after the RF pulse and lasts $t_{\text{acq}} = 800 \mu\text{s}$, with a bandwidth $\text{BW} \approx 45 \text{ kHz}$. The repetition time is $T_{\text{R}} = 280 \text{ ms}$. The k -space undersampling factor is again approximately 8 (870 radial spokes, 18 vertical planes, 176 Cartesian central points). Every image contains 11 averages for a total scan time of approximately 53 min. The bottom row of images in Figure 8A corresponds to scans in which a prepolarization pulse is triggered with a current intensity of approximately 260 A ($B_{\text{t}} \approx 0.56 \text{ T}$), which lasts $t_{\text{p}} = 90 \text{ ms}$ and where $t_{\text{del}1} = 1.5 \text{ ms}$. The pulse sequence for the top row of Figure 8A is identical, but the prepolarization pulse is not triggered ($B_{\text{p}} = 0, B_{\text{t}} = 0.26 \text{ T}$). The ratio $\text{SNR}_{\text{PMRI}}/\text{SNR}_{\text{MRI}}$ yields approximately 1.97, where $\text{SNR}_{\text{PMRI}} \approx 30.95$ and $\text{SNR}_{\text{MRI}} \approx 15.70$ (defined as in the previous paragraph). The expected prepolarization gain from Equation (2) is approximately 2.00.

[†]The undersampling factor here is defined as the ratio of outermost k -space cell areas in the Nyquist and undersampled cases.

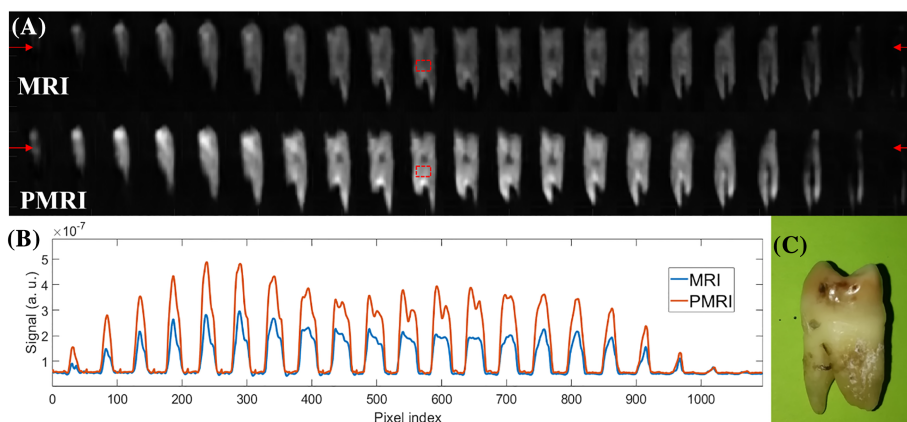


FIGURE 7 A, PETRA (top) and P-PETRA (bottom) images of an ex vivo adult human molar tooth. B, Signal intensity along the horizontal line defined by the red arrows in A. The experimentally obtained value for the prepolarization gain is $\alpha \approx 1.94$ (expected value ≈ 2.02). C, Photograph of the sample

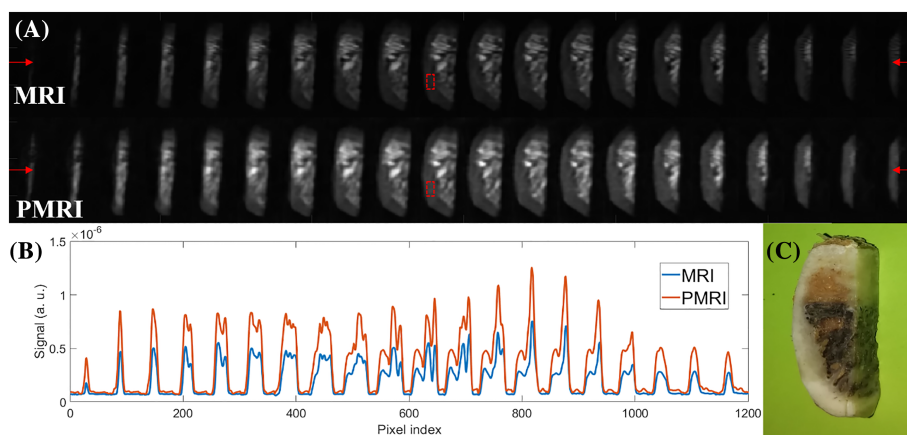


FIGURE 8 A, PETRA (top) and P-PETRA (bottom) images of an ex vivo piece of cattle rib bone. B, Signal intensity along the horizontal line defined by the red arrows in A. The experimentally obtained value for the prepolarization SNR gain is $\alpha \approx 1.97$ (expected value ≈ 2.00). C, Photograph of the sample

6 | DISCUSSION

The preliminary results shown in this work have been obtained in a highly constrained setup in terms of prepolarizer alignment, hydraulic capacity and prepolarizer duty cycle. If the prepolarization field had been aligned with the main static field, we could have approached $B_t = 0.74$ T, leading to an increase in SNR of $\times 2.85$. Also, limitations in the cooling system forced us to work under 260 A, although the system could have taken up to 320 A. This corresponds to $B_t \approx 0.66$ T with the crossed configuration or $B_t \approx 0.87$ T if B_0 and B_p are aligned. In this last situation, we could achieve $\alpha \approx 3.5$ compared to $\alpha \approx 2$ with the actual setup, resulting in a 2.4-fold time reduction for same SNR. On the other hand, working with a prepolarizer field perpendicular to B_0 can be beneficial for faster switching off of B_p and to reduce eddy currents, even if the total B_t is lower. Thus, the benefits of an aligned configuration will largely depend on the ability to reduce eddy currents and to perform a well controlled switch-off of B_p .

A further limitation of our setup is the maximum duty cycle of the GPA 400-750 module, which enforces repetition times $T_R \geq 250$ ms. These are significantly longer than strictly required by the T_1 values of the samples. Assuming a hypothetical $t_p \geq 4T_1$, enough to thermalize at $\approx 98\%$ of the longitudinal magnetization, the T_R could be shortened to around 80 ms for PMRI of teeth (actually, slightly longer due to the increased T_1 time). Increasing the duty cycle can be achieved, for example, by custom fabrication of an efficient cooling system for the high-power gradient amplifier, as compared with the fan-based cooling in our GPA module. This can transfer the total SNR boost into a net gain in SNR per unit time, which is the relevant metric. Taking the example of the human molar tooth and our present setup, a duty cycle defined by $T_R = 80$ instead of 250 ms would translate to the same SNR gain in only approximately 9 min (three times faster). All in all, the combination of prepolarizing at 320 A, $B_0 \parallel B_p$ and $T_R = 80$ ms can shorten the acquisition from 29 to less than 4 min for the image in Figure 7.

Finally, in order to provide a fairer comparison, we could have shortened the MRI sequence by $t_p + t_{\text{off}} + t_{\text{del},1}$. However, if we disregard regimes exploiting steady-state magnetization to shorten the T_R (which is not possible with PMRI), the standard MRI sequence must include a time for thermalization similar to the prepolarization pulse duration. Hence, the two sequences would be comparably long and a prepolarized setup with an optimal duty cycle could lead to a match between $M_{\text{PMRI}}/M_{\text{MRI}}$ and the real SNR boost per unit time.

7 | CONCLUSION AND OUTLOOK

We have demonstrated that it is possible to enhance the quality of magnetic resonance images of hard tissues at low field strengths by means of a high-power prepolarizer module, for a total cost of approximately 20 k€, where the GPA 400-750 module is around 13 k€. The major challenges we have faced are (i) integrating a high-power drive capable of switching off the prepolarization pulse fast enough and (ii) coping with mechanical vibrations due to the strong magnetic interaction between the main and prepolarization fields. We have shown SNR enhancements for *ex vivo* imaging of a human molar tooth (29 min) and a cattle rib bone (53 min) by a factor of approximately 2, although a low duty cycle in the high-power gradient amplifier did not allow us to translate this gain into a real boost in SNR per unit time. Nevertheless, a more efficient dissipation of the heat from the power electronics could lead to a significantly higher duty cycle and therefore to PMRI within shorter scan times.

The results in this paper could be of potential application to clinical dental MRI. While X-rays are commonplace in dental clinics, it is known that they can increase the risk of meningioma and other cancers if performed often.³⁶⁻³⁸ In fact, in recommending X-rays, dentists follow the ALARA principle (as low as reasonably achievable), in direct conflict with medical practice, which would recommend diagnosis and medium-term monitoring as much as required.³⁹ There is, hence, a clear motivation for advances in MRI that aim to replace scanners based on ionizing radiation. Standard (high-field) MRI has proven useful for dentistry, but is too costly for massive use,⁴⁰ and often impractical due to artifacts induced by the magnetic susceptibility of metallic implants.⁴¹ Both problems can be a priori overcome in low-field systems, but the only experimental evidence so far has required excessively long acquisition times.⁹ Hard-tissue PMRI may be a first step towards viable dental MRI. In Section 5 we have demonstrated dental PMRI in 29 min acquisitions. This can be sped up by a factor of 3 or more in our setup with more powerful water cooling for the high-current amplifier (see Section 6), bringing it to scan times under 10 min, albeit in a field of view significantly smaller than a full human jaw. Realistic PMRI in dental practice would seemingly require a combination of techniques, yet to be demonstrated, which could include slice-selective ZTE sequences,²² hybrid filling of the dead-time gap in ZTE,⁴² intra-oral RF detection coils,⁴³ or acceleration schemes based on *k*-space undersampling,⁴⁴ besides exquisite engineering, for scan-time reduction. This constitutes a formidable technical challenge, but holds the promise of safe dental imaging with the added value of soft-tissue visualization.

AUTHOR CONTRIBUTIONS

The high-power electronics for prepolarization were designed and installed by JMG, JB, JPR and JA. The prepolarizer and mechanical holder were designed, assembled and characterized by JPR, JMG, EP and JB, with contributions from DG-R and JA. Experimental data in the “DentMRI—Gen I” scanner were taken by JB and JMG, with help from JMA, FG, RP and JA. Data analysis was performed by JB and JMG, with input from JMA, FG, RP and JA. Animal handling and manipulation of biological tissues were performed by JB. The paper was written by JB, FG and JA, with input from all authors. Experiments were conceived by JMB, JA and AR.

ACKNOWLEDGMENTS

This work was supported by the Ministerio de Ciencia e Innovación of Spain through research grant PID2019-111436RB-C21. Action co-financed by the European Union through the Programa Operativo del Fondo Europeo de Desarrollo Regional (FEDER) of the Comunitat Valenciana 2014–2020 (IDIFEDER/2018/022). JMG and JB acknowledge support from the Innodocto program of the Agencia Valenciana de la Innovación (INNTA3/2020/22 and INNTA3/2021/17).

ETHICAL APPROVAL

All animal parts were obtained from a local butcher and research was conducted following the 3R principles. Experiments using human teeth were approved by the medical center Clínica Llobell Cortell S.L. Procedures were conducted following the approved protocols, and informed consent was obtained from participants prior to study commencement.

CONFLICTS OF INTEREST

JB, JMA, FG, JMB and JA have patents pending that are licensed to Tesoro Imaging S.L. JMB is a co-founder of Tesoro Imaging S.L. JB, JMG, JPR, RB, DG-R and AR are research scientists and engineers at Tesoro Imaging S.L. All other authors declare no competing interests.

DATA AVAILABILITY STATEMENT

The data that support the findings of this study are available from the corresponding author upon reasonable request.

ORCID

Jose Borreguero Morata  <https://orcid.org/0000-0002-6942-312X>

José M. González  <https://orcid.org/0000-0002-5488-7845>

Eduardo Pallás  <https://orcid.org/0000-0001-7791-6592>

Juan P. Rigla  <https://orcid.org/0000-0002-1569-2869>

José M. Algarín  <https://orcid.org/0000-0003-2644-7225>

Rubén Bosch  <https://orcid.org/0000-0002-7316-7819>

Fernando Galve  <https://orcid.org/0000-0002-1600-7341>

Rubén Pellicer  <https://orcid.org/0000-0001-9263-4921>

José M. Benlloch  <https://orcid.org/0000-0001-6073-1436>

Joseba Alonso  <https://orcid.org/0000-0002-2721-1380>

REFERENCES

1. Sarracanie M, LaPierre CD, Salameh N, Waddington DEJ, Witzel T, Rosen MS. Low-cost high-performance MRI. *Sci Rep*. 2015;5(1):15177. <https://www.nature.com/articles/srep15177>
2. Marques JP, Simonis FF, Webb AG. Low-field MRI: an MR physics perspective. *J Magn Reson Imaging*. 2019;49(6):1528-1542. doi:10.1002/jmri.26637
3. Sarracanie M, Salameh N. Low-field MRI: how low can we go? A fresh view on an old debate. *Front Phys*. 2020;8:172. doi:10.3389/fphy.2020.00172/full
4. Macovski A, Conolly S. Novel approaches to low-cost MRI. *Magn Reson Med*. 1993;30(2):221-230.
5. Morgan P, Conolly S, Scott G, Macovski A. A readout magnet for prepolarized MRI. *Magn Reson Med*. 1996;36(4):527-536. doi:10.1002/mrm.1910360405
6. Kegler C, Seton H, Hutchison J. Prepolarized fast spin-echo pulse sequence for low-field MRI. *Magn Reson Med*. 2007;57(6):1180-1184. doi:10.1002/mrm.21238
7. Lee SK, Moessle M, Myers W, et al. MRI: SQUID-detected at 132 μ T with T_1 -weighted contrast established at 10 μ T–300 mT. *Magn Reson Med*. 2005;53(1):9-14. doi:10.1002/mrm.20316
8. Obungoloch J, Harper JR, Consevage S, et al. Design of a sustainable prepolarizing magnetic resonance imaging system for infant hydrocephalus. *Magn Reson Mater Phys Biol Med*. 2018;31(5):665-676. doi:10.1007/s10334-018-0683-y
9. Algarín JM, Díaz-Caballero E, Borreguero J, et al. Simultaneous imaging of hard and soft biological tissues in a low-field dental MRI scanner. *Sci Rep*. 2020;10(1):21470. doi:10.1038/s41598-020-78456-2
10. Rigla JP, Borreguero J, Gramage C, et al. A fast 0.5 T prepolarizer module for preclinical magnetic resonance imaging. *IEEE Trans Magn*. 2021;58:5100208.
11. Kowalewski J, Mäler L. *Nuclear Spin Relaxation in Liquids: Theory, Experiments, and Applications*. Taylor & Francis; 2006.
12. Matter N, Scott G, Grafendorfer T, Macovski A, Conolly S. Rapid polarizing field cycling in magnetic resonance imaging. *IEEE Trans Med Imaging*. 2006;25(1):84-93. <https://ieeexplore.ieee.org/document/1564329/>
13. Matter NI, Scott GC, Venook RD, Ungersma SE, Grafendorfer T, Macovski A, Conolly SM. Three-dimensional prepolarized magnetic resonance imaging using rapid acquisition with relaxation enhancement. *Magn Reson Med*. 2006;56:1085-1095. <http://www.interscience.wiley.com>
14. Venook RD, Matter NI, Ramachandran M, et al. Prepolarized magnetic resonance imaging around metal orthopedic implants. *Magn Reson Med*. 2006;56(1):177-186. doi:10.1002/mrm.20927
15. Savukov I, Karaulanov T. Magnetic-resonance imaging of the human brain with an atomic magnetometer. *Appl Phys Lett*. 2013;103(4):43703. doi:10.1063/1.4816433
16. Inglis B, Buckenmaier K, Sangiorgio P, Pedersen AF, Nichols MA, Clarke J. MRI of the human brain at 130 microtesla. *Proc Natl Acad Sci U S A*. 2013;110(48):19194-19201. <https://www.ncbi.nlm.nih.gov/pubmed/24255111>, <http://www.pubmedcentral.nih.gov/articlerender.fcgi%3Fartid=PMC3845112>
17. Duer MJ. *Introduction to Solid-State NMR Spectroscopy*. Oxford: Blackwell; 2004.
18. Weiger M, Wu M, Wurnig MC, et al. Selective musculoskeletal MRI using ZTE imaging with long-T2 suppression. *Proc Int Soc Magn Reson Med*. 2015;23:941.
19. de Mello RAF, jun Ma Y, Ashir A, et al. Three-dimensional zero echo time magnetic resonance imaging versus 3-dimensional computed tomography for glenoid bone assessment. *Arthroscopy*. 2020;36(9):2391-2400.
20. Seifert AC, Li C, Wilhelm MJ, Wehrli SL, Wehrli FW. Towards quantification of myelin by solid-state MRI of the lipid matrix protons. *NeuroImage*. 2017;163:358-367.
21. Bae K, Jeon KN, Hwang MJ, et al. Respiratory motion-resolved four-dimensional zero echo time (4D ZTE) lung MRI using retrospective soft gating: feasibility and image quality compared with 3D ZTE. *Eur Radiol*. 2020;30(9):5130-5138. doi:10.1007/s00330-020-06890-x
22. Borreguero J, Galve F, Algarín JM, Benlloch JM, Alonso J. Slice-selective zero echo time imaging of ultra-short T2 tissues based on spin-locking. arXiv preprint, p. 2201.06305; 2022.
23. Weiger M, Pruessmann KP, Bracher A-K, et al. High-resolution ZTE imaging of human teeth. *NMR Biomed*. 2012;25(10):1144-1151. doi:10.1002/nbm.2783
24. Hiller T, Dlugosch R, Müller-Petke M. Utilizing pre-polarization to enhance SNMR signals—effect of imperfect switch-off. *Geophys J Int*. 2020;222(2):815-826. doi:10.1093/gji/ggaa
25. Rai R, Manton D, Jameson M, et al. 3D printed phantoms mimicking cortical bone for the assessment of ultrashort echo time magnetic resonance imaging. *Med Phys*. 2017;45:12.
26. Bydder GM, Hajnal JV, Young IR. MRI: use of the inversion recovery pulse sequence. *Clin Radiol*. 1998;53(3):159-176.
27. Carr HY, Purcell EM. Effects of diffusion on free precession in nuclear magnetic resonance experiments. *Phys Rev*. 1954;94(3):630-638.

28. Meiboom S, Gill D. Modified spin-echo method for measuring nuclear relaxation times. *Rev Sci Instrum.* 1958;29(8):688-691.
29. Weiger M, Brunner DO, Dietrich BE, Müller CF, Pruessmann KP. ZTE imaging in humans. *Magn Reson Med.* 2013;70(2):328-332. doi:10.1002/mrm.24816
30. Kobayashi N, Goerke U, Wang L, Ellermann J, Metzger GJ, Garwood M. Gradient-modulated PETRA MRI. *Tomography.* 2015;1(2):85-90. <https://www.mdpi.com/2379-139X/1/2/85>
31. Weiger M, Pruessmann KP. Short-T2 MRI: principles and recent advances. *Prog Nucl Magn Reson Spectrosc.* 2019;114-115:237-270.
32. Grodzki DM, Jakob PM, Heismann B. Ultrashort echo time imaging using pointwise encoding time reduction with radial acquisition (PETRA). *Magn Reson Med.* 2012;67(2):510-518.
33. Karczmarz S. Angenäherte auflösung von systemen linearer gleichungen. *Bull Int Acad Pol Sic Let Cl Sci Math Nat.* 1937:355-357. <https://ci.nii.ac.jp/naid/10009398882/en/>
34. Gower RM, Richtarik P. Randomized iterative methods for linear systems. *SIAM J Matrix Anal Appl.* 2015;36(4):1660-1690.
35. Maggioni M, Katkovnik V, Egiazarian K, Foi A. Nonlocal transform-domain filter for volumetric data denoising and reconstruction. *IEEE Trans Image Process.* 2013;22(1):119-133.
36. Claus EB, Calvocoressi L, Bondy ML, Schildkraut JM, Wiemels JL, Wrensch M. Dental x-rays and risk of meningioma. *Cancer.* 2012;118(18):4530-4537. doi:10.1002/cncr.26625
37. Memon A, Rogers I, Paudyal P, Sundin J. Dental x-rays and the risk of thyroid cancer and meningioma: a systematic review and meta-analysis of current epidemiological evidence. *Thyroid.* 2019;29(11):1572-1593. doi:10.1089/thy.2019.0105
38. Chauhan V, Wilkins RC. A comprehensive review of the literature on the biological effects from dental X-ray exposures. *Int J Radiat Biol.* 2019;95(2):107-119. doi:10.1080/09553002.2019.1547436
39. Jaju PP, Jaju SP. Cone-beam computed tomography: time to move from ALARA to ALADA. *Imaging Sci Dent.* 2015;45(4):263-265. doi:10.5624/isd.2015.45.4.263
40. Mastrogiacomo S, Dou W, Jansen JA, Walboomers XF. Magnetic resonance imaging of hard tissues and hard tissue engineered bio-substitutes. *Mol Imaging Biol.* 2019;21(6):1003-1019. doi:10.1007/s11307-019-01345-2
41. Gao X, Wan Q, Gao Q. Susceptibility artifacts induced by crowns of different materials with prepared teeth and titanium implants in magnetic resonance imaging. *Sci Rep.* 2022;12(1):428. <https://www.nature.com/articles/s41598-021-03962-w>
42. Froidaveaux R, Weiger M, Rösler MB, Brunner DO, Pruessmann KP. HYFI: hybrid filling of the dead-time gap for faster zero echo time imaging. *NMR Biomed.* 2021;34(6):e4493. doi:10.1002/nbm.4493
43. Ludwig U, Eisenbeiss AK, Scheifele C, et al. Dental MRI using wireless intraoral coils. *Sci Rep.* 2016;6.
44. Lustig M, Donoho D, Pauly JM, Sparse MRI. The application of compressed sensing for rapid MR imaging. *Magn Reson Med.* 2007;58(6):1182-1195. doi:10.1002/mrm.21391

How to cite this article: Borreguero Morata J, González JM, Pallás E, et al. Prepolarized MRI of hard tissues and solid-state matter. *NMR in Biomedicine.* 2022;35(8):e4737. doi:10.1002/nbm.4737